Physics and Chemistry of Minerals (2018) 45:945–962
https://doi.org/10.1007/s00269-018-0976-8

ORIGINAL PAPER

High-pressure behavior of intermediate scapolite: compressibility, structure deformation and phase transition

Paolo Lotti[1] · Davide Comboni[1] · Marco Merlini[1] · Michael Hanfland[2]

Received: 24 March 2018 / Accepted: 9 May 2018 / Published online: 21 May 2018

Abstract

Scapolites are common volatile-bearing minerals in metamorphic rocks. In this study, the high-pressure behavior of an intermediate member of the scapolite solid solution series (Me_{47}), chemical formula $(Na_{1.86}Ca_{1.86}K_{0.23}Fe_{0.01})(Al_{4.36}Si_{7.64})O_{24}[Cl_{0.48}(CO_3)_{0.48}(SO_4)_{0.01}]$, has been investigated up to 17.79 GPa, by means of in situ single-crystal synchrotron X-ray diffraction. The isothermal elastic behavior of the studied scapolite has been described by a III-order Birch–Murnaghan equation of state, which provided the following refined parameters: $V_0 = 1110.6(7)$ Å^3, $K_{V_0} = 70(2)$ GPa ($\beta_{V_0} = 0.0143(4)$ GPa^{-1}) and $K'_V = 4.8(7)$. The refined bulk modulus is intermediate between those previously reported for Me_{17} and Me_{68} scapolite samples, confirming that the bulk compressibility among the solid solution increases with the Na content. A discussion on the *P*-induced structure deformation mechanisms of tetragonal scapolite at the atomic scale is provided, along with the implications of the reported results for the modeling of scapolite stability. In addition, a single-crystal to single-crystal phase transition, which is displacive in character, has been observed toward a triclinic polymorph at 9.87 GPa. The high-pressure triclinic polymorph was found to be stable up to the highest pressure investigated.

Keywords Scapolite · Compressibility · Phase transition · Synchrotron X-ray diffraction

Introduction

Scapolite represents a non-binary solid solution series, whose members can be rock-forming minerals in crustal igneous and metamorphic environments. The general chemical formula of scapolite can be written as $M_4[T_{12}O_{24}]A$, where M is a monovalent or divalent cation, usually Na^+, Ca^{2+} (major components), K^+, Sr^{2+}, Ba^{2+} or Fe^{2+}; T represents Si^{4+} and Al^{3+} (less commonly Fe^{3+}) in tetrahedral coordination; A is an anion, usually Cl^-, CO_3^{2-} or SO_4^{2-}. Three end-members have been reported: marialite, $Na_4Al_3Si_9O_{24}Cl$, and meionite, $Ca_4Al_6Si_6O_{24}(CO_3)$, are long-time known (Shaw 1960), whereas silvialite, $Ca_4Al_6Si_6O_{24}(SO_4)$, the sulfate analogue of meionite, has been described only recently (Teerstra et al. 1999). A common symbolism adopted to define the scapolite composition is that of meionite content, Me_X, which, in its broadest definition, is $Me_X = \Sigma(M^{2+})/\Sigma(M^+ + M^{2+})$. The complex substitution mechanisms operating across the solid solution series have been thoroughly studied. Evans et al. (1969) proposed two substitutional schemes: between marialite (Me_0) and Me_{75} and between Me_{75} and meionite (Me_{100}). The same substitutional schemes have been reported by Chamberlain et al. (1985) and Hassan and Buseck (1988). Zolotarev (1993, 1996), based on new chemical analyses of scapolite samples and on revision of the literature data, proposed the existence of three binary solid solutions among the end-members marialite and meionite: (1) from $Na_4Al_3Si_9O_{24}Cl$ to $CaNa_3Al_4Si_8O_{24}Cl$, (2) from $CaNa_3Al_4Si_8O_{24}Cl$ to $NaCa_3Al_5Si_7O_{24}CO_3$ and (3) from $NaCa_3Al_5Si_7O_{24}CO_3$ to $Ca_4Al_6Si_6O_{24}CO_3$. The existence of three binary solid solution series was later confirmed by means of spectroscopic (NMR), powder and single-crystal X-ray diffraction analyses (Sokolova et al. 1996; Sheriff et al. 1998, 2000; Sokolova and Hawthorne 2008). As noted by Sokolova and Hawthorne

Electronic supplementary material The online version of this article (https://doi.org/10.1007/s00269-018-0976-8) contains supplementary material, which is available to authorized users.

✉ Paolo Lotti
paolo.lotti@unimi.it

[1] Dipartimento di Scienze della Terra, Università degli Studi di Milano, Via Botticelli 23, 20133 Milan, Italy

[2] European Synchrotron Radiation Facility, 71 Avenue des Martyrs, CS 40220, 38043 Grenoble Cedex 9, France

(2008), due to the complex substitution mechanisms within the scapolite series, the Me_X symbolism reported above is not formally correct, but is effective to roughly define the scapolite composition and valid at a first approximation. For this reason, it will be adopted hereafter to refer to samples of this and previous studies. A further complex feature of scapolite minerals concerns their symmetry: the compounds close to the marialite end-member, on one side, and to the meionite end member, on the other side, are usually found to crystallize with a structure described in the *I*4/*m* space group, whereas the intermediate members have $P4_2/n$ symmetry. Hawthorne and Sokolova (2008) placed the occurrence of the phase transitions at Me_{20} and Me_{75}, respectively, and ascribed it to the coupling of the short range order between the $[(Si,Al)_{12}O_{24}]$ and {Na,Ca}{Cl,(CO_3)} frameworks.

The crystal structure of scapolite was first solved by Pauling (1930) and Schiebold and Seumel (1932) and refined by several authors (e.g., Papike and Stephenson 1966; Lin and Burley 1973a). In the *I*4/*m* space group, two independent tetrahedral sites occur, T1 and T2, which give rise to an open-framework analogue to that of feldspathoids and zeolites (Fig. 1). In the $P4_2/n$ structure, T2 splits into two independent sites, i.e., T2 and T3. In the *I*4/*m* members close to the marialite side of the series, Al is strongly ordered at the T2 site, whereas at the composition corresponding to the phase transition to $P4_2/n$, Al is strongly concentrated at T2 and depleted at T3. With increasing meionite content, Al fills both T1 and T3, until a similar content at T2 and T3 is reached and the *I*4/*m* structure is recovered, close to the meionite-rich side of the series, where a preferential ordering of Al at T2, with respect to T1, is still preserved (Sokolova and Hawthorne 2008). The (Si,Al)-tetrahedra give rise to two different four-membered rings: type-I (hereafter 4mR-I), made by the T1 tetrahedra, and type-II (hereafter 4mR-II), made by T2/T3 tetrahedra (Fig. 1). Their interconnection along the [001] direction builds up columns of five-membered rings of tetrahedra. The latter and the 4mR-I define a large structural cage, centered on the fourfold axis and hosting the anions (either Cl, CO_3 or SO_4) (Fig. 1). The access to the cage is granted by four symmetry-related eight-membered rings of tetrahedra (Fig. 1). Along the direction parallel to the **c** axis, i.e., [001], every cage is surrounded by four symmetry-related highly elliptical channels defined by eight-membered rings of tetrahedra (hereafter $8mR_{[001]}$, Fig. 1). These channels host the cations, occupying, both in *I*4/*m* and $P4_2/n$, one independent site (Fig. 1). Every anion in the cage is therefore surrounded by four cations, whereas every cation is bonded to seven framework oxygens (Fig. 2) and to one anion (one bond with Cl, one or two bonds with the carbonate or sulfate oxygens).

In nature, scapolites are typical minerals of metamorphic environments. CO_3- and SO_4-rich members are commonly

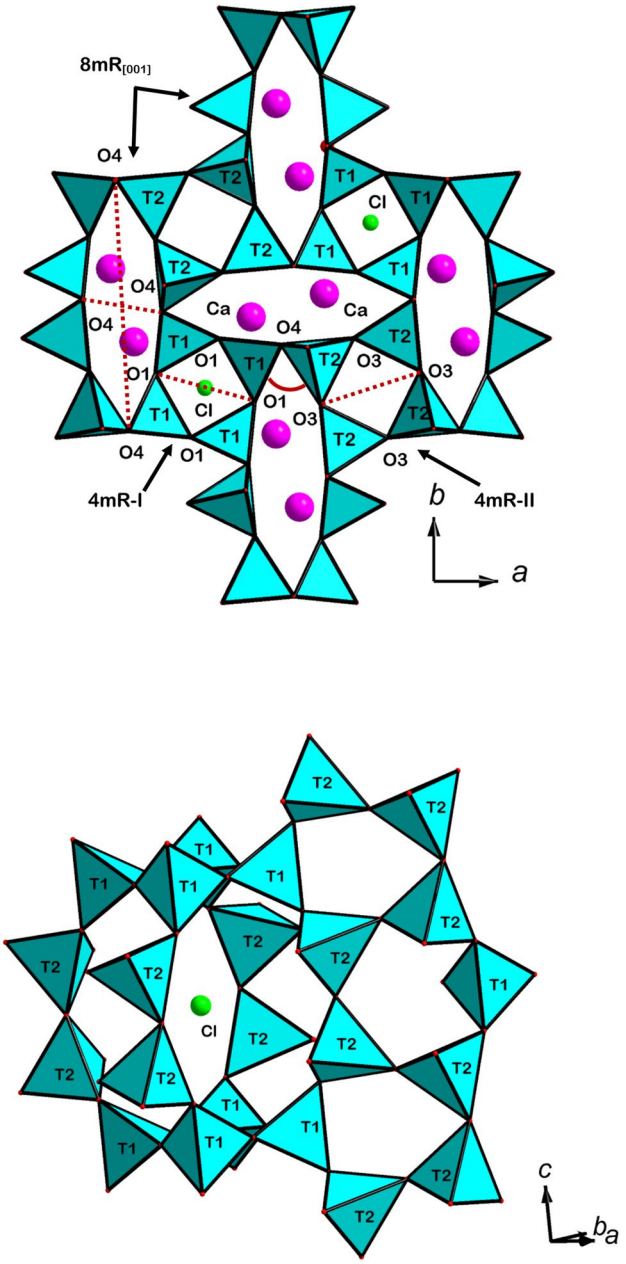

Fig. 1 (*Up*) View of the scapolite crystal structure (in the *I*4/*m* space group) along the **c** crystallographic axis. Relevant structural parameters are reported. (*Down*) View of the structural cage hosting the anions (only Cl is shown for an ease of clarity)

reported as constituents of metamorphic rocks in amphibolite and granulite facies (Oterdoom and Wenk 1983; Satish-Kumar et al. 2006; Porter and Austrheim 2017; Hammerli et al. 2017), but are also reported to be unstable during the regression to lower grade metamorphic facies (Satish-Kumar et al. 2006; Porter and Austrheim 2017; Hammerli et al. 2017). Cl-rich scapolites are reported in a broader range of metamorphic environments, from greenschist to eclogite facies (Frietsch et al. 1997; Kullerud and Erambert 1999;

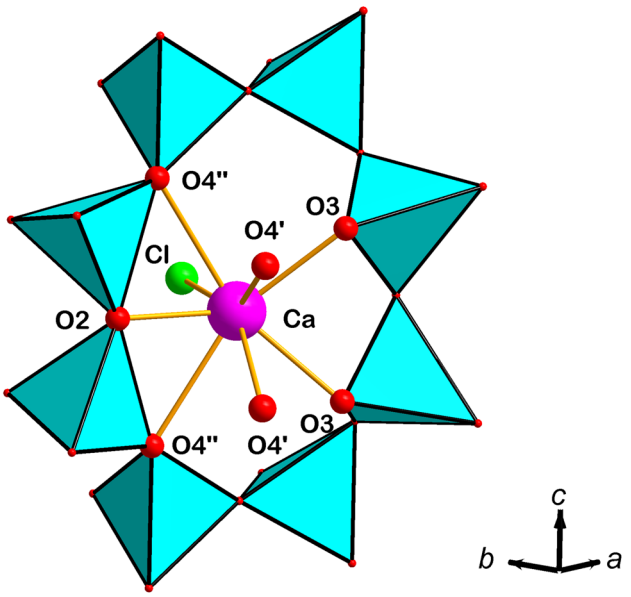

Fig. 2 View of the coordination environment of the cation site in the tetragonal polymorph of scapolite

Satish-Kumar et al. 2006; Katongo et al. 2011), including contact (Arranz et al. 2002; Mazhari et al. 2011) and hydrothermal metamorphism (Frietsch et al. 1997; Bernal et al. 2017). Although less commonly, scapolites of magmatic origin have also been reported (Smith et al. 2008) and is noteworthy to mention that scapolite has also been found within a melt inclusion in olivine from a martian meteorite (Filiberto et al. 2014). Overall, scapolites usually form at non-ambient temperature and pressure conditions in presence of plagioclase and fluids carrying Cl^-, CO_3^{2-} and/or SO_4^{2-} anions. Therefore, scapolite has been reported in the literature as an important reservoir of volatiles within the Earth's crust (e.g., Satish-Kumar et al. 2006; Porter and Austrheim 2017; Hammerli et al. 2017). In addition, Cl-rich scapolites of hydrothermal origin are often associated with ore minerals deposits (Frietsch et al. 1997; Katongo et al. 2011; Almeida and Jenkins 2017), whereas the destabilization of SO_4-rich scapolites during metamorphic regression may release a significant amount of sulfur, which, in turn, may influence the fractionation and concentration of chalcophile elements (Porter and Austrheim 2017; Hammerli et al. 2017). For these reasons, several experimental investigations have been devoted to understand the relative stability of scapolite with respect to plagioclase, halite, calcite and/or volatile-bearing fluids (e.g., Orville 1975; Ellis 1978; Baker and Newton 1995; Almeida and Jenkins 2017). At the same time, the quantitative characterization of the elastic and structural behavior of the members across the scapolite series, at varying temperature and pressure conditions, is equally important for understanding the stability and occurrence of these minerals in metamorphic environments. Levien and Papike (1976), Graziani and Lucchesi (1982) and Baker (1994) reported the high-temperature behavior (at ambient *P*) of several members of the scapolite series, remarking a significant elastic anisotropy and the role played by the chemical composition. Hazen and Sharp (1988) and Comodi et al. (1990) reported the high-pressure behavior (at ambient *T*) of three members of the solid solution (Me_{88}, Me_{68} and Me_{17}) up to ca. 4 GPa, pointing out that an increase in the meionite content is coupled with a decrease in the bulk compressibility.

In this study, we have investigated the high-*P* (and ambient-*T*) behavior of an intermediate scapolite (Me_{47}) up to ca. 18 GPa, by means of in situ high-*P* single-crystal synchrotron X-ray diffraction, using diamond anvil cells. A comparative analysis with the literature data (Hazen and Sharp 1988; Comodi et al. 1990) is provided. In addition, we report, for the first time, the occurrence a tetragonal-to-triclinic phase transition at ca. 9.5 GPa.

Materials and experimental methods

A gem-quality and transparent single crystal of scapolite from Madagascar, ca. 1 cm in diameter, belonging to a private mineralogical collection, has been chosen for this experiment. Several fragments of the starting single crystal were recovered and investigated under the polarized microscope to check the absence of optical defects and inclusions.

Four of the largest fragments were selected for the chemical analysis, which was performed using a Jeol JXA-8200 electron microprobe, operating in wavelength-dispersive mode (EPMA-WDS), at the Earth Sciences Department of the University of Milano (ESD-MI), Italy. The system was operated with an accelerated voltage of 15 kV, a beam current of 5 nA, a counting time of 30 s on the peaks and 10 s on the backgrounds and a beam diameter of 3 μm. Natural samples have been used as standards for calibration: grossular for Si, Al and Ca, omphacite for Na, K-feldspar for K, celestite for Sr, fayalite for Fe, galena for S and marialitic scapolite for Cl. The results of chemical analysis are reported in Table 1.

A single-crystal fragment, ca. $300 \times 200 \times 200$ μm^3 in size, was selected for a single-crystal X-ray diffraction data collection at ambient conditions using an Oxford Diffraction Xcalibur four-circle diffractometer at the ESD-MI, equipped with a Mo-Kα X-ray tube, a graphite monochromator and a CCD detector, and operating at 50 kV and 30 mA. A combination of ϕ and ω scans, with 1°/frame step width and 20 s/frame exposure time, was adopted to maximize the reciprocal lattice coverage. Indexing of the diffraction peaks, refinement of the unit-cell parameters and intensity data reduction were performed using the CrysAlisPro version 1.171.38.46 software system (Rigaku Oxford Diffraction

Table 1 Composition of four selected fragments from the investigated single-crystal sample of scapolite

wt%	# 1	s.d. (# 1)	# 2	s.d. (# 2)	# 3	s.d. (# 3)	# 4	s.d. (# 4)
SiO_2	51.97	0.41	51.56	0.43	50.43	0.27	51.65	0.39
Al_2O_3	24.61	0.26	24.95	0.14	25.37	0.11	24.63	0.17
FeO	0.05	0.03	0.05	0.03	0.04	0.02	0.04	0.02
CaO	11.48	0.44	11.49	0.18	12.37	0.08	11.25	0.05
MgO	0.01	0.01	0.02	0.01	0.01	0.01	0.02	0.01
BaO	0.01	0.01	0.01	0.01	0.04	0.02	0.01	0.01
SrO	0.08	0.05	0.04	0.02	0.03	0.01	0.04	0.02
MnO	0.02	0.01	0.01	0.01	0.01	0.01	0.01	0.01
Na_2O	6.61	0.23	6.49	0.06	6.10	0.07	6.57	0.10
K_2O	1.24	0.08	1.25	0.03	1.10	0.02	1.27	0.01
SO_3	0.08	0.01	0.07	0.02	0.08	0.05	0.07	0.03
Cl	1.87	0.01	1.94	0.02	1.72	0.02	1.92	0.04
O=Cl	−0.43		−0.45		−0.40		−0.46	
Sum	98.01		97.43		96.90		97.02	
CO_2[a]	2.71		2.24		2.53		2.26	
apfu								
Si	7.70		7.64		7.53		7.68	
Al	4.30		4.36		4.47		4.32	
Fe	0.01		0.01		0.01		0.01	
Ca	1.82		1.83		1.98		1.79	
Mg	0.00		0.00		0.00		0.00	
Ba	0.00		0.00		0.00		0.00	
Sr	0.01		0.00		0.00		0.00	
Mn	0.00		0.00		0.00		0.00	
Na	1.90		1.87		1.77		1.89	
K	0.23		0.24		0.21		0.24	
S	0.01		0.01		0.01		0.01	
Cl	0.48		0.50		0.45		0.50	
C	0.51		0.45		0.52		0.46	

The composition of each fragment is based on five-point analyses

[a]Calculated according to the protocol of Teerstra and Sheriff (1997), assuming that (1) it is the amount necessary to compensate the excess positive charge obtained subtracting the framework and anions negative charges from the sum of cations charges, and (2) the investigated sample is anhydrous

2018). Corrections for the crystal absorption were applied by the semiempirical ABSPACK routine implemented in CrysAlisPro.

The in situ high-pressure single-crystal X-ray diffraction experiments were performed, using a diamond anvil cell, at the former ID09A beamline of the European Synchrotron Radiation Facility (ESRF, Grenoble, France). A monochromatic X-ray beam ($E = 30$ keV, $\lambda = 0.4138$ Å) has been focused on the samples (beam size = 30×30 μm^2) and the X-ray diffraction patterns have been collected by a MAR555 flat panel detector at 250 mm from the sample position. A description of the beamline experimental setup can be found in Merlini and Hanfland (2013). A single crystal fragment, ca $30 \times 20 \times 20$ μm^3 in size was selected for the experiment and loaded in the *P*-chamber obtained, by electro spark erosion (hole diameter = 250 μm), in a pre-indented (to ~ 70 μm) steel foil gasket. A mixture of methanol:ethanol:water (16:3:1, hereafter mew) was used as *P*-transmitting medium (Angel et al. 2007) and the ruby-fluorescence method (Mao et al. 1986; Chervin et al. 2001) was adopted for pressure calibration. A remotely controlled membrane-driven diamond anvil cell, with Boehler–Almax designed diamonds (culet diameter = 600 μm) was used. Eighteen intensity data collections (two of which in decompression) were performed at different pressures from ambient conditions (crystal in the DAC without *P*-medium) up to 10.23 GPa. The same collection strategy was always applied: an ω-scan from −30° to +30°, with 1° step width and 1 s exposure time per frame.

Since a phase transition was detected between 9.23 and 9.87 GPa (see "Phase transition from tetragonal to triclinic scapolite"), which is close to the hydrostatic limit of the adopted *P*-transmitting fluid mixture (Angel et al. 2007),

a second high-pressure ramp was performed using helium as *P*-transmitting medium. The same experimental conditions as those reported above were adopted using a single-crystal fragment of similar size and shape, except for the following: a pre-indented (to ~ 45 μm) rhenium foil was used as a gasket and a hole, 100 μm in diameter, was drilled by spark-erosion to serve as *P*-chamber, as Boehler–Almax designed diamonds with 300 μm culet size were used. Nineteen intensity data collections (one of which in decompression) were performed at different pressures from 0.20 up to 17.79 GPa using the same ω-scan strategy described above. For both the H*P*-ramps, indexing, refinement of the unit-cell parameters and intensity data reduction were performed using the CrysAlisPro software (Rigaku Oxford Diffraction 2018). Corrections for absorption of the DAC components were performed using the ABSPACK routine implemented in CrysAlisPro. Unit-cell parameters pertaining to both the *P*-ramps are reported in Tables S1 and S2 (deposited as supplementary materials).

Structure refinements

All the structure refinements have been performed using the JANA2006 software (Petříček et al. 2014).

Scapolites with compositions between ~ Me_{20} and Me_{75} are always reported to crystallize in the tetragonal space group $P4_2/n$ (cf. Lin and Burley 1973b, 1975; Sherriff et al. 1998; Sokolova and Hawthorne 2008). However, our single-crystal X-ray diffraction data, collected both at ambient conditions using a conventional diffractometer and at high pressure using synchrotron radiation ("Materials and experimental methods"), always showed the occurrence of systematic extinctions consistent with an *I*-centered lattice (Fig. 3). A discussion on this point is given in the "Crystal chemistry and structure of the investigated scapolite". For this reason, according to the observed systematic extinctions, the structure refinement based on the intensity data collected at ambient conditions at the ESD-MI was performed in the *I*4/*m* space group, starting from the framework coordinates of the S6 sample reported by Sokolova and Hawthorne (2008). The cations and anions sites have been subsequently detected by the position of residual peaks in the difference-Fourier maps of the electron density. In the final cycles of the refinement all, but the anions sites, have been refined using anisotropic displacement parameters (hereafter adps). The X-ray scattering curve of Si was assigned to the T1 and T2 tetrahedral sites. The Na, Ca and K sites were restrained to share the same coordinates and adps and their fractional occupancies were restrained so that their sum would be one. The refinement of the Cl^- and CO_3^{2-} anions in the structural cage was less straightforward, due to the strong correlations arising by their close positions in the average structure model. Therefore, in order to minimize correlations, the Cl, C and the three Oc sites were restrained to share the same isotropic displacement parameter (hereafter idp), the C and Oc sites to share the same fractional occupancy, the C–O bond lengths were retrained to 1.30 ± 0.02 Å and the O–C–O bond angles of the carbonate group were restrained to 120° ± 2°. The final cycles converged with no significant correlations among the refined parameters. Statistical parameters pertaining to the structure refinement are reported in Table 2.

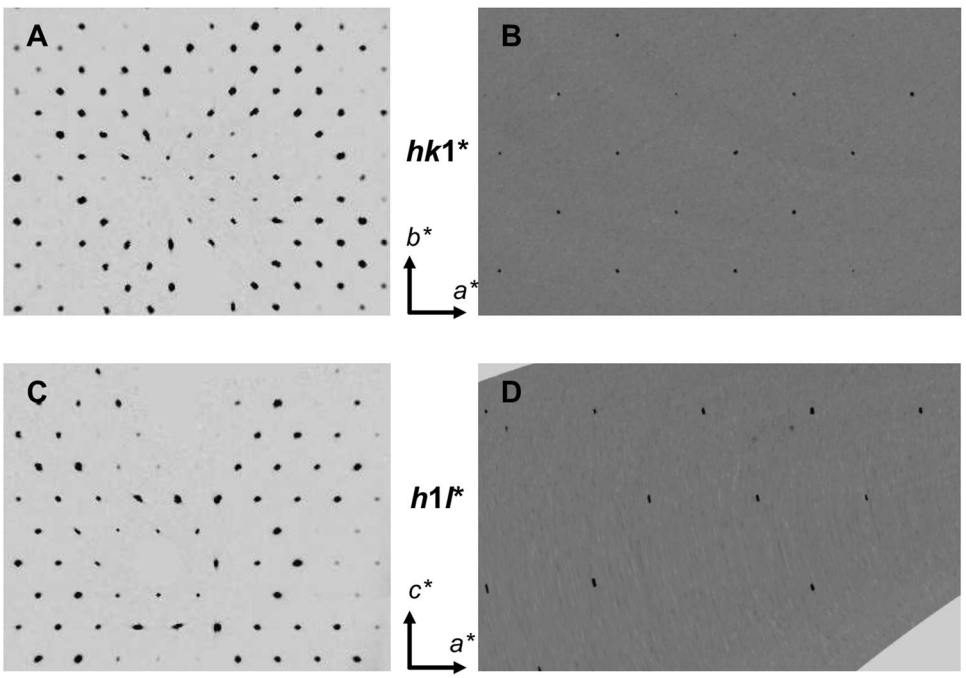

Fig. 3 Reconstructions of selected reciprocal lattice planes of the tetragonal polymorph of scapolite, based on the single-crystal X-ray diffraction data collected at ambient conditions at the Earth Sciences Department of the University of Milano (**A, C**) and at 0.20 GPa (with the crystal in the DAC) at the European Synchrotron Radiation Facility (**B, D**). Further details are in "Materials and experimental methods"

Table 2 Details pertaining to the structure refinements of the tetragonal and triclinic polymorphs of scapolite, at different pressures

P (GPa)	0.0001	0.0001*	0.15(2)	0.67(2)	1.29(2)	1.83(2)	2.46(2)	3.24(2)	3.80(2)	4.48(2)	5.27(2)
Experiment	Air ESD-MI	H*P*-mew	H*P*-mew	H*P*-mew	H*P*-mew	H*P*-mew	H*P*-mew	H*P*-mew	H*P*-mew	H*P*-mew	H*P*-mew
Space group	*I*4/*m*	*I*4/*m*	*I*4/*m*	*I*4/*m*	*I*4/*m*	*I*4/*m*	*I*4/*m*	*I*4/*m*	*I*4/*m*	*I*4/*m*	*I*4/*m*
min ≤ *h*, *k*, *l* ≤ max	−16 ≤ *h* ≤ 16 −16 ≤ *k* ≤ 16 −9 ≤ *l* ≤ 10	−19 ≤ *h* ≤ 19 −18 ≤ *k* ≤ 19 −4 ≤ *l* ≤ 4	−18 ≤ *h* ≤ 19 −17 ≤ *k* ≤ 17 −5 ≤ *l* ≤ 4	−19 ≤ *h* ≤ 18 −17 ≤ *k* ≤ 17 −5 ≤ *l* ≤ 4	−19 ≤ *h* ≤ 18 −17 ≤ *k* ≤ 17 −5 ≤ *l* ≤ 4	−18 ≤ *h* ≤ 19 −17 ≤ *k* ≤ 16 −5 ≤ *l* ≤ 4	−19 ≤ *h* ≤ 18 −17 ≤ *k* ≤ 16 −5 ≤ *l* ≤ 4	−19 ≤ *h* ≤ 18 −17 ≤ *k* ≤ 16 −5 ≤ *l* ≤ 4	−19 ≤ *h* ≤ 18 −17 ≤ *k* ≤ 16 −5 ≤ *l* ≤ 4	−18 ≤ *h* ≤ 19 −16 ≤ *k* ≤ 17 −5 ≤ *l* ≤ 4	−19 ≤ *h* ≤ 18 −17 ≤ *k* ≤ 16 −5 ≤ *l* ≤ 4
Unique reflections	765	466	469	467	432	460	421	424	421	443	412
Observed reflections $F_o^2/\sigma(F_o^2) > 3$	703	366	377	378	351	367	348	347	349	362	335
R_{int} (all)	0.0242	0.0502	0.0534	0.0519	0.0438	0.0448	0.0443	0.0416	0.0417	0.0454	0.0510
Refined param	63	58	58	58	58	58	58	58	58	58	58
R_1 (obs)	0.0380	0.0565	0.0471	0.0701	0.0500	0.0514	0.0575	0.0603	0.0550	0.0551	0.0718
R_1 (all)	0.0427	0.0710	0.0593	0.0806	0.0612	0.0606	0.0678	0.0731	0.0655	0.0659	0.0830
wR_1 (obs)	0.0591	0.0659	0.0542	0.0773	0.0581	0.0575	0.0643	0.0685	0.0615	0.0622	0.0786
Residuals (e^-/Å^3)	+0.68 −1.01	+0.63 −0.74	+0.61 −0.62	+1.04 −1.13	+0.78 −0.78	+0.79 −0.91	+0.83 −0.77	+0.90 −0.88	+0.94 −0.82	+0.96 −0.70	+1.18 −1.05
P (GPa)	6.03(2)	6.75(2)	7.63(2)	8.49(2)	9.23(2)	1.34(2)[d]	0.20(2)	1.09(2)	2.02(2)	3.06(2)	3.97(2)
Experiment	H*P*-mew	H*P*-mew	H*P*-mew	H*P*-mew	H*P*-mew	H*P*-mew	H*P*-He	H*P*-He	H*P*-He	H*P*-He	H*P*-He
Space group	*I*4/*m*	*I*4/*m*	*I*4/*m*	*I*4/*m*	*I*4/*m*	*I*4/*m*	*I*4/*m*	*I*4/*m*	*I*4/*m*	*I*4/*m*	*I*4/*m*
min ≤ *h*, *k*, *l* ≤ max	−18 ≤ *h* ≤ 19 −17 ≤ *k* ≤ 16 −5 ≤ *l* ≤ 4	−19 ≤ *h* ≤ 18 −16 ≤ *k* ≤ 17 −5 ≤ *l* ≤ 4	−19 ≤ *h* ≤ 18 −16 ≤ *k* ≤ 17 −5 ≤ *l* ≤ 4	−19 ≤ *h* ≤ 18 −16 ≤ *k* ≤ 16 −5 ≤ *l* ≤ 4	−18 ≤ *h* ≤ 18 −16 ≤ *k* ≤ 17 −5 ≤ *l* ≤ 4	−17 ≤ *h* ≤ 18 −16 ≤ *k* ≤ 17 −5 ≤ *l* ≤ 3	−7 ≤ *h* ≤ 10 −17 ≤ *k* ≤ 16 −7 ≤ *l* ≤ 8	−10 ≤ *h* ≤ 9 −16 ≤ *k* ≤ 16 −6 ≤ *l* ≤ 8	−8 ≤ *h* ≤ 10 −16 ≤ *k* ≤ 17 −7 ≤ *l* ≤ 8	−9 ≤ *h* ≤ 8 −16 ≤ *k* ≤ 17 −7 ≤ *l* ≤ 8	−8 ≤ *h* ≤ 9 −17 ≤ *k* ≤ 16 −7 ≤ *l* ≤ 8
Unique reflections	440	439	399	388	424	415	477	420	478	477	464
Observed reflections $F_o^2/\sigma(F_o^2) > 3$	357	356	322	304	294	374	359	330	374	364	317
R_{int} (all)	0.0577	0.0509	0.0344	0.0373	0.0385	0.0804	0.0385	0.0376	0.0430	0.0325	0.0353
Refined param	58	58	58	58	58	58	61	61	61	61	61
R_1 (obs)	0.0600	0.0593	0.0562	0.0560	0.0599	0.0876	0.0490	0.0462	0.0535	0.0455	0.0526
R_1 (all)	0.0721	0.0717	0.0688	0.0690	0.0832	0.0916	0.0625	0.0589	0.0663	0.0611	0.0779
wR_1 (obs)	0.0675	0.0661	0.0643	0.0622	0.0654	0.1065	0.0614	0.0534	0.0675	0.0572	0.0574
Residuals (e^-/Å^3)	+1.08 −0.92	+1.00 −0.83	+0.92 −0.93	+0.76 −0.77	+0.78 −0.74	+1.21 −1.32	+0.70 −0.72	+0.57 −0.65	+0.68 −0.83	+0.60 −0.78	+0.64 −0.61

Table 2 (continued)

P (GPa)	5.09(2)	6.12(2)	7.00(2)	8.17(2)	9.02(2)	10.08(2)	11.06(2)	12.30(2)	13.39(2)	14.61(2)	0.28[d](2)
Experiment	HP-He	HP-He	HP-He	HP-He	HP-He	HP-He	HP-He	HP-He	HP-He	HP-He	HP-He
Space group	*I*4/*m*	*I*4/*m*	*I*4/*m*	*I*4/*m*	*I*4/*m*	$I\bar{1}$	$I\bar{1}$	$I\bar{1}$	$I\bar{1}$	$I\bar{1}$	*I*4/*m*
min ≤ *h*, *k*, *l* ≤ max	$-10 \le h \le 9$ $-17 \le k \le 16$ $-9 \le l \le 7$	$-9 \le h \le 8$ $-16 \le k \le 17$ $-7 \le l \le 8$	$-8 \le h \le 9$ $-17 \le k \le 16$ $-7 \le l \le 8$	$-8 \le h \le 9$ $-16 \le k \le 16$ $-9 \le l \le 7$	$-8 \le h \le 9$ $-16 \le k \le 16$ $-7 \le l \le 8$	$-9 \le h \le 10$ $-16 \le k \le 16$ $-7 \le l \le 7$	$-9 \le h \le 10$ $-16 \le k \le 15$ $-7 \le l \le 7$	$-9 \le h \le 10$ $-16 \le k \le 15$ $-7 \le l \le 7$	$-8 \le h \le 10$ $-16 \le k \le 15$ $-7 \le l \le 7$	$-9 \le h \le 10$ $-16 \le k \le 15$ $-6 \le l \le 7$	$-9 \le h \le 10$ $-17 \le k \le 17$ $-7 \le l \le 8$
Unique reflections	506	453	451	439	429	385	498	446	439	423	464
Observed reflections $F_o^2/\sigma(F_o^2) > 3$	388	343	343	319	295	269	324	346	346	289	309
R_{int} (all)	0.0371	0.0315	0.0444	0.0340	0.0407	0.1033	0.1059	0.1057	0.0672	0.0428	0.0547
Refined param	61	61	61	61	61	106	106	106	106	106	61
R_1 (obs)	0.0466	0.0512	0.0543	0.0514	0.0610	0.1116	0.1222	0.1254	0.1117	0.1215	0.0695
R_1 (all)	0.0586	0.0676	0.0716	0.0709	0.0845	0.1564	0.1606	0.1478	0.1310	0.1496	0.0918
wR_1 (obs)	0.0596	0.0596	0.0649	0.0578	0.0660	0.1150	0.1355	0.1358	0.1254	0.1318	0.0703
Residuals ($e^-/Å^3$)	+0.72 −0.78	+0.79 −0.85	+0.82 −0.80	+0.61 −0.86	+0.77 −0.84	+0.55 −0.53	+0.73 −0.64	+0.62 −0.73	+0.49 −0.46	+0.53 −0.46	+0.65 −0.68

*With the crystal in the DAC without *P*-medium

Fractional coordinates, occupancies and dps are reported in Table 3. Selected structural parameters are reported in Table 4 and Table S3 (deposited as supplementary material).

The structure refinements based on the intensity data collected at high-*P* before the phase transition (i.e., low-*P* polymorph) were performed in the *I*4/*m* space group, starting from the model described above. In addition, to the same restrictions previously reported, the occupancies of the Ca, Na, K, Cl, C and Oc sites have been constrained according to the measured chemical composition (Table 1). The refinements based on the high-*P* data in mew were performed restraining the displacement parameter of the O2 atom to be isotropic, as any attempt of anisotropic refinement failed, likely for insufficient information due to the shadowing of portions of the reciprocal lattice by the DAC components (see e.g., Miletich et al. 2000).

The structure refinements of the high-pressure polymorph were performed in the triclinic *I*-1 subgroup (see "Phase transition from tetragonal to triclinic scapolite"), based on the intensity data collected in He at 10.08, 11.06, 12.30, 13.39 and 14.61 GPa. At higher pressures, a dramatic reduction in the number of observed reflections (i.e., $F^2_{hkl}/\sigma(F^2_{hkl}) \ge 3$) prevented robust and reliable structure refinements. In order to compensate the increase in the number of independent variables, due to symmetry reduction, all the independent atomic positions have been refined with idps. Fractional occupancies of cationic and anionic sites were constrained according to the measured chemical composition and assumed to be identical among the independent sites with a common parent site in *I*4/*m*. In addition, the same restraints previously described were applied.

Statistical parameters on the structure refinements based on high-*P* data are reported in Table 2, whereas fractional coordinates, occupancies and dps from selected pressures are reported in Table 3. Selected structural parameters are reported in Table 4 and S3. The volumes of coordination polyhedra have been calculated using the tools implemented in the software *Vesta* (Momma and Izumi 2011).

Results

Chemical composition

The chemical composition of four fragments of the large single-crystal selected for this experiment, determined by EPMA-WDS, is reported in Table 1. For any fragment, the reported mass fractions have been averaged from five-point analyses. The chemical formula has been calculated, according to the method proposed by Teerstra and Sheriff (1997), normalizing to Si + Al = 12 atoms per formula unit (apfu). The CO_2 content, following the protocol of Teerstra and Sheriff (1997), has been calculated assuming that:

Table 3 Site occupancy factors (s.o.f.), coordinates and isotropic or equivalent displacement parameters (Å^2) from selected structure refinements of tetragonal and triclinic scapolite

Site	Experiment	P (GPa)	s.o.f.	x	y	z	U_{iso}/U_{eq}
Tetragonal scapolite							
Ca	Air-ESD-MI	0.0001	0.35(8)	0.3605(1)	0.28524(9)	0	0.0276(4)
	H*P*-He	0.20(2)	0.465	0.3616(2)	0.2858(2)	0	0.0286(9)
	H*P*-He	5.09(2)	0.465	0.3652(2)	0.2878(2)	0	0.0279(8)
	H*P*-He	9.02(2)	0.465	0.3689(3)	0.2907(2)	0	0.047(1)
Na	Air-ESD-MI	0.0001	0.49(8)	*	*	*	*
	H*P*-He	0.20(2)	0.465	*	*	*	*
	H*P*-He	5.09(2)	0.465	*	*	*	*
	H*P*-He	9.02(2)	0.465	*	*	*	*
K	Air-ESD-MI	0.0001	0.16(8)	*	*	*	*
	H*P*-He	0.20(2)	0.058	*	*	*	*
	H*P*-He	5.09(2)	0.058	*	*	*	*
	H*P*-He	9.02(2)	0.058	*	*	*	*
T1	Air-ESD-MI	0.0001	1.0	0.16120(7)	0.09055(8)	0	0.0068(3)
	H*P*-He	0.20(2)	1.0	0.1611(2)	0.0911(2)	0	0.0063(6)
	H*P*-He	5.09(2)	1.0	0.1597(2)	0.0974(2)	0	0.0081(5)
	H*P*-He	9.02(2)	1.0	0.1589(2)	0.1001(2)	0	0.0187(8)
T2	Air-ESD-MI	0.0001	1.0	0.16000(6)	0.41420(6)	0.2069(1)	0.0096(2)
	H*P*-He	0.20(2)	1.0	0.1610(1)	0.4140(1)	0.2067(2)	0.0092(5)
	H*P*-He	5.09(2)	1.0	0.1607(1)	0.4087(1)	0.2070(2)	0.0113(4)
	H*P*-He	9.02(2)	1.0	0.1605(2)	0.4071(2)	0.2075(3)	0.0242(7)
O1	Air-ESD-MI	0.0001	1.0	0.0419(2)	0.1500(2)	0	0.0147(7)
	H*P*-He	0.20(2)	1.0	0.0423(4)	0.1497(5)	0	0.015(2)
	H*P*-He	5.09(2)	1.0	0.0381(4)	0.1541(4)	0	0.018(2)
	H*P*-He	9.02(2)	1.0	0.0365(5)	0.1552(6)	0	0.045(3)
O2	Air-ESD-MI	0.0001	1.0	0.1901(2)	0.3767(2)	0	0.0157(8)
	H*P*-He	0.20(2)	1.0	0.1898(5)	0.3760(5)	0	0.014(2)
	H*P*-He	5.09(2)	1.0	0.1877(4)	0.3675(4)	0	0.018(2)
	H*P*-He	9.02(2)	1.0	0.1868(6)	0.3623(5)	0	0.034(3)
O3	Air-ESD-MI	0.0001	1.0	0.1506(2)	0.5515(2)	0.2112(3)	0.0182(6)
	H*P*-He	0.20(2)	1.0	0.1502(3)	0.5515(3)	0.2120(6)	0.017(1)
	H*P*-He	5.09(2)	1.0	0.1535(3)	0.5488(3)	0.2059(5)	0.020(1)
	H*P*-He	9.02(2)	1.0	0.1543(4)	0.5474(4)	0.2034(8)	0.040(2)
O4	Air-ESD-MI	0.0001	1.0	0.2309(2)	0.1309(2)	0.1736(3)	0.0177(6)
	H*P*-He	0.20(2)	1.0	0.2312(4)	0.1318(3)	0.1735(5)	0.016(1)
	H*P*-He	5.09(2)	1.0	0.2293(3)	0.1387(3)	0.1758(5)	0.021(1)
	H*P*-He	9.02(2)	1.0	0.2287(5)	0.1419(4)	0.1768(7)	0.042(2)
Cl	Air-ESD-MI	0.0001	0.44(1)	0.5	0.5	0	0.061(2)
	H*P*-He	0.20(2)	0.48	0.5	0.5	0	0.055(3)
	H*P*-He	5.09(2)	0.48	0.5	0.5	0	0.042(2)
	H*P*-He	9.02(2)	0.48	0.5	0.5	0	0.043(3)
C	Air-ESD-MI	0.0001	0.14(1)	0.515(2)	0.513(2)	0	**
	H*P*-He	0.20(2)	0.12	0.525(4)	0.502(7)	0	**
	H*P*-He	5.09(2)	0.12	0.527(3)	0.502(4)	0	**
	H*P*-He	9.02(2)	0.12	0.523(4)	0.506(5)	0	**
Oc1	Air-ESD-MI	0.0001	0.14(1)	0.470(3)	0.608(3)	0	**
	H*P*-He	0.20(2)	0.12	0.469(6)	0.593(10)	0	**
	H*P*-He	5.09(2)	0.12	0.460(4)	0.588(6)	0	**
	H*P*-He	9.02(2)	0.12	0.454(5)	0.593(9)	0	**
Oc2	Air-ESD-MI	0.0001	0.14(1)	0.424(3)	0.544(4)	0	**
	H*P*-He	0.20(2)	0.12	0.406(10)	0.523(9)	0	**

Table 3 (continued)

Site	Experiment	*P* (GPa)	s.o.f.	*x*	*y*	*z*	U_{iso}/U_{eq}
	H*P*-He	5.09(2)	0.12	0.399(5)	0.512(6)	0	**
	H*P*-He	9.02(2)	0.12	0.403(7)	0.516(8)	0	**
Oc3	Air-ESD-MI	0.0001	0.14(1)	0.493(3)	0.620(3)	0	**
	H*P*-He	0.20(2)	0.12	0.494(4)	0.632(4)	0	**
	H*P*-He	5.09(2)	0.12	0.482(4)	0.636(3)	0	**
	H*P*-He	9.02(2)	0.12	0.476(4)	0.633(3)	0	**
Triclinic scapolite							
Ca_1	H*P*-He	10.08(2)	0.465	0.379(3)	0.2935(8)	0.057(3)	0.052(3)
Na_1	H*P*-He	10.08(2)	0.465	#	#	#	#
K_1	H*P*-He	10.08(2)	0.058	#	#	#	#
Ca_3	H*P*-He	10.08(2)	0.465	−0.289(3)	0.3686(9)	−0.013(3)	0.062(4)
Na_3	H*P*-He	10.08(2)	0.465	##	##	##	##
K_3	H*P*-He	10.08(2)	0.058	##	##	##	##
T1_1	H*P*-He	10.08(2)	1.0	0.159(2)	0.1030(7)	−0.003(2)	0.027(2)
T1_3	H*P*-He	10.08(2)	1.0	−0.090(2)	0.1588(6)	0.017(2)	0.029(2)
T2_1	H*P*-He	10.08(2)	1.0	0.144(2)	0.4214(7)	0.195(2)	0.039(3)
T2_2	H*P*-He	10.08(2)	1.0	−0.176(2)	−0.3953(7)	0.208(2)	0.034(3)
T2_3	H*P*-He	10.08(2)	1.0	−0.397(2)	0.1469(7)	0.200(2)	0.033(2)
T2_4	H*P*-He	10.08(2)	1.0	0.417(2)	−0.1724(7)	0.207(2)	0.035(3)
O1_1	H*P*-He	10.08(2)	1.0	0.045(2)	0.165(2)	0.064(4)	0.035(6)
O1_3	H*P*-He	10.08(2)	1.0	−0.137(4)	0.031(1)	0.028(5)	0.032(6)
O2_1	H*P*-He	10.08(2)	1.0	0.195(4)	0.361(2)	0.011(3)	0.044(6)
O2_3	H*P*-He	10.08(2)	1.0	−0.352(3)	0.186(2)	−0.001(3)	0.056(8)
O3_1	H*P*-He	10.08(2)	1.0	0.128(7)	0.562(1)	0.170(7)	0.040(6)
O3_2	H*P*-He	10.08(2)	1.0	−0.180(3)	−0.538(1)	0.214(4)	0.029(5)
O3_3	H*P*-He	10.08(2)	1.0	−0.535(2)	0.135(2)	0.212(5)	0.048(7)
O3_4	H*P*-He	10.08(2)	1.0	0.556(2)	−0.162(2)	0.208(4)	0.063(9)
O4_1	H*P*-He	10.08(2)	1.0	0.257(3)	0.117(3)	0.154(5)	0.11(2)
O4_2	H*P*-He	10.08(2)	1.0	−0.208(4)	−0.152(2)	0.192(5)	0.040(6)
O4_3	H*P*-He	10.08(2)	1.0	−0.148(3)	0.242(2)	0.171(4)	0.049(7)
O4_4	H*P*-He	10.08(2)	1.0	0.122(3)	−0.213(1)	0.186(3)	0.580(8)
Cl_1	H*P*-He	10.08(2)	0.48	0.5	0.5	0	0.049(9)
C_1	H*P*-He	10.08(2)	0.12	0.54(3)	0.50(2)	0.01(5)	###
Oc1_1	H*P*-He	10.08(2)	0.12	0.48(2)	0.59(3)	0.02(7)	###
Oc2_1	H*P*-He	10.08(2)	0.12	0.47(3)	0.43(1)	0.15(3)	###
Oc3_1	H*P*-He	10.08(2)	0.12	0.58(3)	0.62(2)	0.14(4)	###
C_3	H*P*-He	10.08(2)	0.12	−0.49(3)	0.57(1)	0.02(3)	###
Oc1_3	H*P*-He	10.08(2)	0.12	−0.56(2)	0.49(1)	0.09(4)	###
Oc2_3	H*P*-He	10.08(2)	0.12	−0.51(5)	0.40(3)	−0.06(7)	###
Oc3_3	H*P*-He	10.08(2)	0.12	−0.64(3)	0.51(2)	−0.09(4)	###

*Ca, Na and K restrained to share the same coordinates and anisotropic dps; **Cl, C, Oc1, Oc2 Oc3 restrained to share the same isotropic dps; see "Structure refinements" for further details; #Ca_1, Na_1 and K_1 restrained to share the same coordinates and isotropic dps; ##Ca_3, Na_3 and K_3 restrained to share the same coordinates and isotropic dps; ###Cl_1, C_1, C_3, Oc1_1, Oc2_1, Oc3_1, Oc1_3, Oc2_3 and Oc3_3 restrained to share the same isotropic dps; see "Structure refinements" for further details

(1) it is the amount necessary to compensate the excess positive charge obtained subtracting the framework and anions (Cl^- and SO_4^{2-}) negative charges from the sum of cations charge, and (2) the investigated scapolite sample is anhydrous.

As there is no significant difference among the compositions of the investigated fragments, an average chemical formula can be calculated: $(Na_{1.86}Ca_{1.86}K_{0.23}Fe_{0.01})(Al_{4.36}Si_{7.64})O_{24}[Cl_{0.48}(CO_3)_{0.48}(SO_4)_{0.01}]$. The chemical analysis shows that the investigated sample is intermediate

Table 4 Selected angles (°), distances (Å) and volumes (Å^3) from the refined structure models of tetragonal scapolite at different pressures

Experiment	*P* (GPa)	O1–O4–O3	$8mR_{[001]}$ O4–O4 short	$8mR_{[001]}$ O4–O4 long	$8mR_{[001]}$ ε^b	4mR-I O1–O1	4mR-II O3–O3	<T1-O>	*V*(T1)	<T2-O>	*V*(T2)	*V*(Ca)[c]
Air ESD-MI	0.0001	93.60(6)	3.144(3)	9.318(3)	0.3374(4)	3.776(4)	3.858(3)	1.625(3)	2.199(4)	1.670(3)	2.378(4)	19.1(2)
H*P*-mew	0.0001[a]	93.7(1)	3.130(7)	9.325(6)	0.3357(7)	3.763(7)	3.855(6)	1.628(7)	2.215(9)	1.670(5)	2.375(7)	19.1(11)
H*P*-mew	0.15(2)	93.57(9)	3.137(5)	9.318(4)	0.3367(7)	3.775(6)	3.856(4)	1.624(5)	2.197(8)	1.670(4)	2.379(6)	19.1(7)
H*P*-mew	0.67(2)	93.1(1)	3.101(7)	9.318(6)	0.3328(9)	3.755(7)	3.840(6)	1.619(7)	2.18(1)	1.668(5)	2.365(8)	19.0(10)
H*P*-mew	1.29(2)	92.6(1)	3.054(6)	9.319(6)	0.3277(7)	3.763(6)	3.851(6)	1.621(5)	2.186(8)	1.668(4)	2.366(7)	18.6(8)
H*P*-mew	1.83(2)	92.2(1)	3.026(5)	9.307(6)	0.3251(8)	3.760(6)	3.843(4)	1.621(5)	2.183(7)	1.665(4)	2.353(7)	18.4(8)
H*P*-mew	2.46(2)	91.7(1)	2.987(6)	9.321(6)	0.320(1)	3.763(7)	3.843(6)	1.620(6)	2.181(9)	1.663(5)	2.347(8)	18.2(9)
H*P*-mew	3.24(2)	91.4(1)	2.964(7)	9.308(6)	0.3184(8)	3.747(7)	3.835(6)	1.614(7)	2.16(1)	1.662(5)	2.340(8)	18.0(10)
H*P*-mew	3.80(2)	91.1(1)	2.938(6)	9.305(6)	0.3157(8)	3.749(7)	3.828(6)	1.614(6)	2.155(9)	1.659(4)	2.329(7)	17.9(9)
H*P*-mew	4.48(2)	90.9(1)	2.924(6)	9.288(6)	0.315(1)	3.743(6)	3.825(6)	1.608(6)	2.133(9)	1.659(4)	2.327(7)	17.7(9)
H*P*-mew	5.27(2)	90.6(1)	2.900(9)	9.279(7)	0.313(1)	3.730(9)	3.809(7)	1.604(8)	2.12(1)	1.656(6)	2.316(9)	17.5(11)
H*P*-mew	6.03(2)	90.3(1)	2.877(7)	9.265(6)	0.311(1)	3.746(7)	3.814(6)	1.602(7)	2.11(1)	1.655(5)	2.309(8)	17.4(10)
H*P*-mew	6.75(2)	89.9(1)	2.846(7)	9.262(6)	0.307(1)	3.734(7)	3.811(5)	1.600(7)	2.10(1)	1.651(5)	2.292(8)	17.2(10)
H*P*-mew	7.63(2)	89.7(1)	2.810(7)	9.245(7)	0.304(1)	3.727(7)	3.805(5)	1.607(7)	2.13(1)	1.648(5)	2.279(8)	17.0(10)
H*P*-mew	8.49(2)	89.6(1)	2.804(7)	9.239(7)	0.304(1)	3.709(7)	3.783(5)	1.594(7)	2.08(1)	1.646(5)	2.270(8)	17.0(10)
H*P*-mew	9.23(2)	89.5(1)	2.793(7)	9.207(7)	0.303(1)	3.700(7)	3.782(7)	1.587(7)	2.05(1)	1.640(6)	2.248(9)	16.9(10)
H*P*-He	0.20(2)	93.57(8)	3.117(6)	9.319(7)	0.3345(9)	3.763(7)	3.841(6)	1.624(6)	2.196(8)	1.667(4)	2.365(6)	19.1(8)
H*P*-He	1.09(2)	92.63(8)	3.067(6)	9.309(6)	0.3295(9)	3.771(7)	3.877(6)	1.624(5)	2.197(7)	1.668(4)	2.365(5)	18.7(8)
H*P*-He	2.02(2)	92.22(8)	3.022(6)	9.314(7)	0.3245(9)	3.769(7)	3.835(6)	1.618(6)	2.170(8)	1.665(4)	2.354(6)	18.4(7)
H*P*-He	3.06(2)	91.61(8)	2.969(6)	9.297(6)	0.3194(9)	3.758(7)	3.819(6)	1.616(5)	2.162(7)	1.659(4)	2.330(5)	18.1(8)
H*P*-He	3.97(2)	91.08(9)	2.926(6)	9.300(7)	0.3146(8)	3.766(7)	3.801(6)	1.614(6)	2.158(8)	1.656(4)	2.318(6)	18.0(7)
H*P*-He	5.09(2)	90.63(9)	2.900(6)	9.282(6)	0.3124(9)	3.758(7)	3.814(6)	1.610(5)	2.141(7)	1.656(4)	2.315(5)	17.6(8)
H*P*-He	6.12(2)	90.29(9)	2.871(6)	9.269(7)	0.310(1)	3.759(7)	3.794(7)	1.606(6)	2.123(8)	1.654(4)	2.306(5)	17.5(8)
H*P*-He	7.00(2)	89.93(9)	2.834(7)	9.260(7)	0.306(1)	3.760(7)	3.782(7)	1.605(6)	2.118(8)	1.649(5)	2.286(6)	17.4(8)
H*P*-He	8.17(2)	89.63(9)	2.812(7)	9.237(7)	0.304(1)	3.744(7)	3.779(7)	1.598(6)	2.090(8)	1.645(5)	2.271(6)	17.1(9)
H*P*-He	9.02(2)	89.49(9)	2.787(7)	9.223(9)	0.302(1)	3.721(9)	3.767(7)	1.595(7)	2.080(9)	1.642(6)	2.254(8)	17.0(9)

[a]Sample in the DAC without *P*-medium

[b]$\varepsilon = O4\text{–}O4_{short}/O4\text{–}O4_{long}$

[c]Fictive volume defined as <Ca–Of>^{3}, see "High-pressure behavior of intermediate scapolite" for further details

between the end-members marialite and meionite, with an insignificant amount of sulfate anions. According to the symbolism of meionite content reported in "Introduction", the sample of this study can be classified as Me_{47}.

The cations composition from the structure refinement based on the data collected in air at the ESD-MI (Table 3) shows an overestimation in K and an underestimation in Ca, which can be attributed to their similar X-ray scattering factors. Nevertheless, the calculated electrons content (per unit formula) from cations based on the structure refinement (i.e., 61.72 e^-), is in fair agreement to that calculated from the experimental chemical formula (i.e., 62.29 e^-). For this reason, the cations occupancies in the structure refinements based on the high-*P* data have been fixed to the values derived from the chemical analysis (Tables 1, 3).

High-pressure elastic behavior of tetragonal scapolite

The *P*-induced evolution of the unit-cell parameters of the tetragonal polymorph of scapolite, obtained from both the *P*-ramps in mew and He, are reported in Table S1 and in Fig. 4, from which a different elastic behavior along the **a** and **c** axes is observed. At ambient conditions, the compressibility is highest within the (001) plane and lowest along the direction parallel to the fourfold axis, i.e., [001]. However, if a stiffening is observed with pressure along the **a** axis, a softening affects the **c** axis at $P > 2.00$–2.50 GPa, as confirmed by the *P*-induced behavior of the *c*/*a* ratio reported in Fig. 4 and Table S1. In addition, a sudden increase in compressibility affects the structure along both the crystallographic directions and, in turn, the bulk elastic behavior at $P > 8.50$ GPa, likely ascribable to the impending phase transition (see "Phase transition from tetragonal to triclinic scapolite").

An isothermal Birch–Murnaghan equation of state, truncated to the third order (hereafter III-BM EoS), which is widely used to model the isothermal bulk elastic behavior of minerals (Birch 1947; Duffy and Wang 1998; Angel 2000), has been fitted to the experimental *V*–*P* data of tetragonal scapolite in the range 0.0001–8.49 GPa (i.e., excluding the points showing the anomalous increase in compressibility at $P > 8.50$ GPa), using the *EoSFit7_GUI* software (Angel et al. 2014; Gonzalez-Platas et al. 2016). The obtained refined parameters are: $V_0 = 1110.6(7)$ Å^3, $K_{V0} = 70(2)$ GPa ($\beta_{V0} = 0.0143(4)$ GPa^{-1}) and $K'_V = 4.8(7)$, where $K_{V0} = 1/\beta_{V0}$, $\beta_{V0} = -1/V \cdot (\partial V/\partial P)_T$ and $K'_V = \partial K_V/\partial P$. A fit of the *V*–*P* data with a BM-EoS truncated to the second order (II-BM EoS), for which K'_V is fixed to 4, has also been performed, for an ease of comparison with the literature data: $V_0 = 1110.1(5)$ Å^3 and $K_{V0} = 72.4(7)$ GPa.

P-induced structure deformation of tetragonal scapolite

The *P*-induced bulk compression of open-framework silicates, both zeolites and feldspathoids, is usually accommodated by the tilting of the rigid framework tetrahedra (see e.g., Gatta and Lee 2014; Lotti et al. 2015a, b, 2016; Gatta and Lotti 2016; Comboni et al. 2017; Gatta et al. 2018) and this is the main mechanism operating also in the investigated sample of scapolite. However, a slight compression of the independent T1 and T2 tetrahedra can also be observed (Table 4). Interestingly, a subtle increase in the compressibility of the T2 tetrahedron (Fig. 5) can be detected at $P > 4$ GPa. The main deformation mechanism accommodating compression and expansion in the plane perpendicular to the tetragonal axis, i.e., (001), is governed by the cooperative rotation of the 4mRs around the shared O4 oxygen hinges (Fig. 1), as previously reported by Levien and Papike (1976) and Comodi et al. (1990). This mechanism leads to a decrease in ellipticity of the $8mR_{[001]}$ with temperature and an increase in ellipticity with pressure. A comparative analysis of the refined structure models, based on the high-*P* data from both the ramps in mew and He, shows that such a cooperative rotation, described by the closure of the O1–O4–O3 intertetrahedral angle (Figs. 1; Table 4), induces an increase in ellipticity, mainly governed by the compression of the shortest O4-O4 diameter of the $8mR_{[001]}$ channels (Figs. 1, 5; Table 4). However, at $P > 4$ GPa a sudden increase in the compressibility of the longest O4-O4 diameter is also observed (Figs. 1, 5; Table 4). The compression within the (001) plane is also partly accommodated by the internal compression of the 4mRs-II (Fig. 1), which can be described by the shortening of the O3–O3 diameter (Fig. 1; Table 4). On the other hand, the 4mR-I apparently undergoes an internal compression (shortening of O1–O1) only at pressures close to the destabilization of the tetragonal polymorph of scapolite (Fig. 1; Table 4). It is interesting to note that the 4mR-I delimits, in the plane perpendicular to [001], the cage hosting the anionic groups. The access to that cage in the plane parallel to [001] is defined by 8mRs (Fig. 1), whose height corresponds to the **c** unit-cell axis, and therefore undergoes an increase in compressibility at *P* ca. > 2 GPa. Overall, the high-*P* behavior of the structure along the **c** unit-cell axis (Fig. 4, Table S1) and of the 4mR-I (Table 4) imply a continuous increase in the compressibility of the structural cage hosting the anionic groups.

The cations filling the 8mR channels are bonded to 7 oxygen atoms (Fig. 2). Hereafter, the notation "Ca" will be adopted to refer to the cation site, shared by either Ca, Na, or K. The high-pressure behavior of the Ca–O bonds is reported in Fig. 5 and Table S3, where it is shown that a linear compression of the Ca–O3 and Ca–O4″ bonds occurs within the entire range of stability of the tetragonal scapolite,

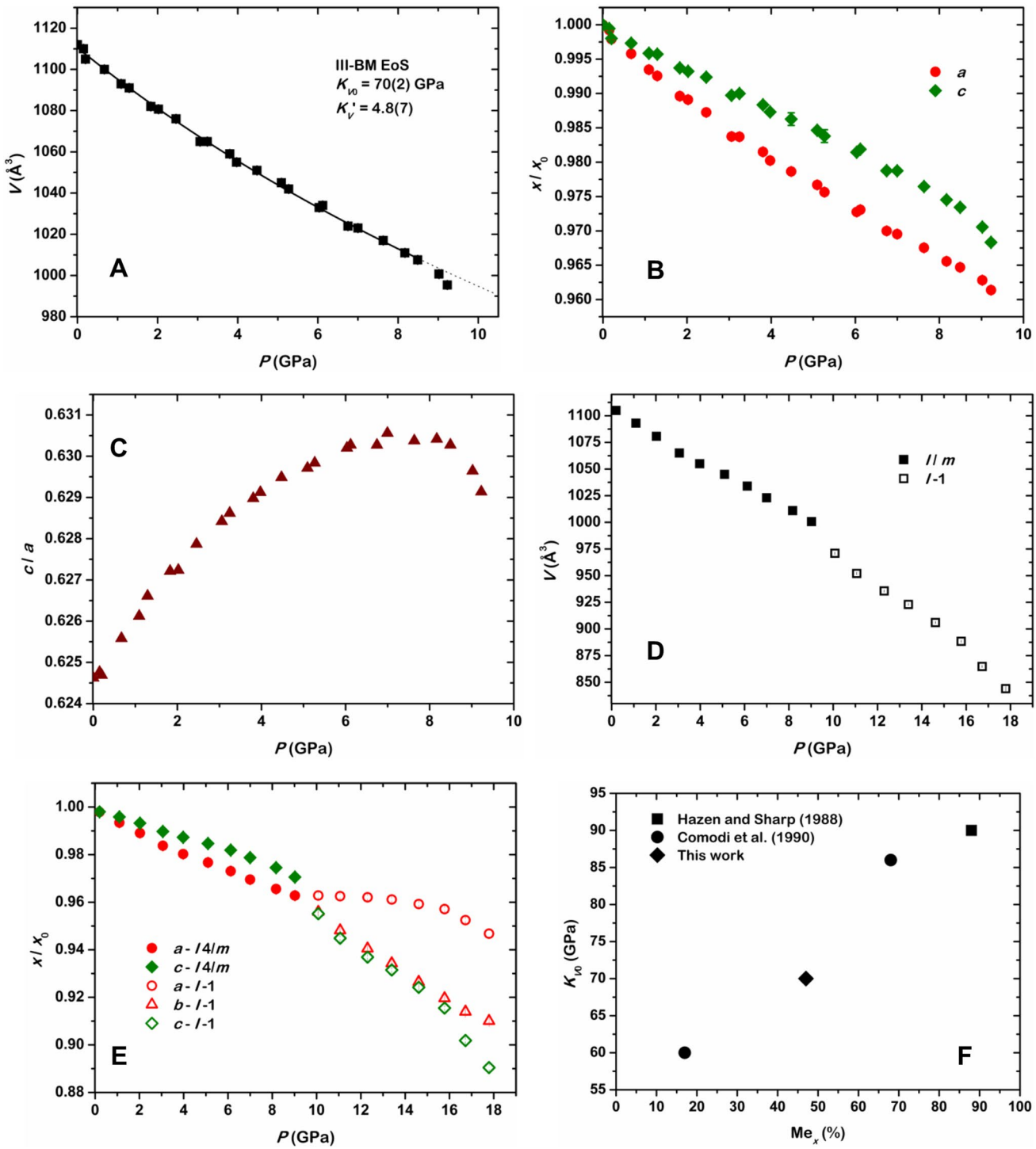

Fig. 4 **A** High-pressure evolution of the unit-cell volume of tetragonal scapolite, based on the data from both the ramps with mew and He as *P*-transmitting fluids, respectively. The refined III-BM EoS is shown. **B** *P*-induced evolution of the unit-cell parameters *a* and *c* (normalized to the ambient condition values) of tetragonal scapolite. **C** Unit-cell *c*/*a* ratio of tetragonal scapolite as a function of pressure. **D, E** *P*-induced evolution of the unit-cell volumes and normalized linear parameters of the tetragonal and triclinic polymorphs of scapolite, based on the data from the He ramp. **F** Refined bulk moduli of four members of the scapolite solid solution series as a function of the meionite content (defined as in "Introduction")

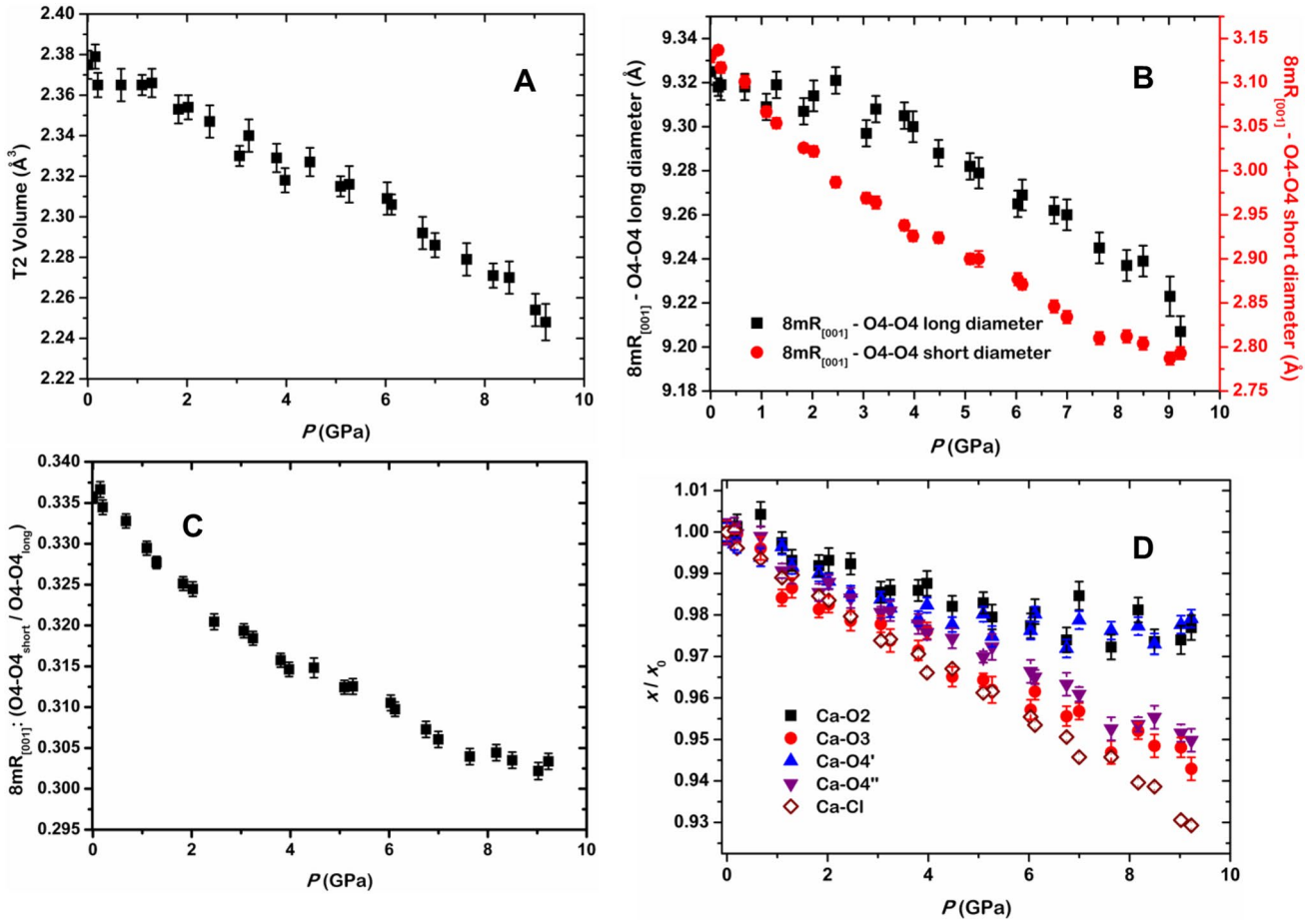

Fig. 5 **A** Volume of the T2 coordination polyhedron as a function of pressure. **B** High-pressure evolution of the $8mR_{[001]}$ channel diameters. **C** The $8mR_{[001]}$ channel ellipticity (defined as $O4–O4_{short}/O4–O4_{long}$) as a function of pressure. **D** *P*-induced evolution of the Ca–O and Ca–Cl bond lengths (normalized to the ambient-conditions values). All the diagrams refer to tetragonal scapolite

whereas the Ca–O2 and Ca–O4′ bonds undergo a saturation at $P > 4$ GPa. A perfect linear compressibility, within the stability range of the tetragonal polymorph, is also shown by the Ca–Cl bonds (Fig. 2 and Table S3). On the other hand, we avoided any description of the high-*P* behavior of the interatomic bonds between the cations and the oxygens of the carbonate group, due to the potential bias induced by the significant restraints applied to the C and Oc sites during the structure refinements.

Phase transition from tetragonal to triclinic scapolite

A phase transition, displacive in character and apparently of the first order, from the starting tetragonal scapolite towards a polymorph with triclinic symmetry has been observed both in the *P*-ramp in mew, between 9.23 and 9.87 GPa, and in the ramp in He, between 9.02 and 10.08 GPa. For an ease of comparison with the tetragonal *I*4/*m* crystal structure, the triclinic polymorph has not been described in the primitive reduced cell, but in the $I\bar{1}$ space group, as in this way the tetragonal and triclinic unit cells are directly comparable. For both the *P*-ramps, the data collections performed in decompression showed that the tetragonal-to-triclinic phase transition is fully reversible.

Following the phase transition, the T1 and T2 tetrahedral sites split into two (T1_1 and T1_3) and four (T2_1, T2_2, T2_3 and T2_4) independent crystallographic sites, respectively. However, the three-dimensional framework may still be described as made by one 4mR defined by the T1 tetrahedra (4mR-I) and one 4mR defined by the T2 tetrahedra (4mR-II, Fig. 6), but the symmetry reduction removes the constraints induced by the fourfold axis. As a consequence, both the rings are significantly distorted in the triclinic polymorph, the 4mR-I being approximately elongated along the *a* axis and the 4mR-II along the *b* axis, respectively (Fig. 6). The symmetry reduction makes different (i.e., not equivalent) the $8mR_{[001]}$ channels. In the triclinic polymorph, two sets of independent channels exist: one set roughly elongated

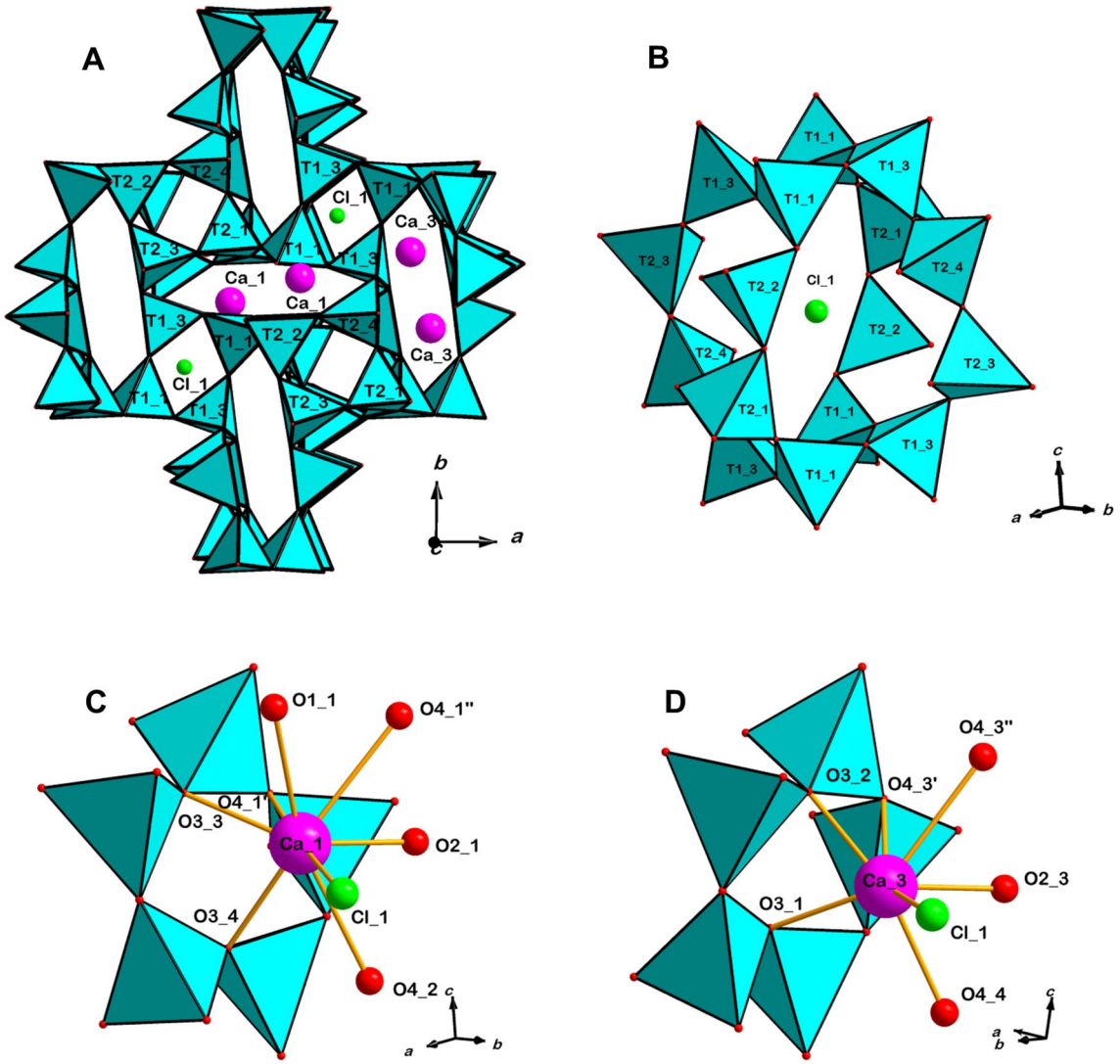

Fig. 6 **A** Crystal structure of the triclinic polymorph of scapolite viewed down the **c** crystallographic axis. **B** The structural cage hosting the anions in triclinic scapolite. **C, D** View of the coordination environment of the Ca_1 and Ca_3 cation sites of triclinic scapolite

along [100] and the second set roughly elongated along [010] (Fig. 6). Each set of channels is made by the alternation of two independent 8mRs and, therefore, in the $I\bar{1}$ scapolite four independent $8mR_{[001]}$ exist. The structural cage is delimited by the distorted 4mR-I in the plane roughly perpendicular to [001] and by two sets of independent 8mR channels, roughly perpendicular to the [100] and [010] directions, respectively (Fig. 6), and is characterized by a significant deformation.

The Cl atom still occupies one independent site in the triclinic polymorph, whereas the CO_3 sites have been derived according to the $I4/m$->$I\bar{1}$ group–subgroup relationships, as any trial to locate them by means of difference-Fourier syntheses failed. The cation site splits into two independent positions: Ca_1 occupies the channels roughly elongated along [100], whereas Ca_3 is located in the channels approximately elongated along [010] (Fig. 6). With respect to the tetragonal polymorph, cations in Ca_1 also make seven bonds with the framework oxygens, but after losing a bond with one of the farther O4″ atoms and gaining a bond with O1_1 (Fig. 6); Ca_3 only loses a bond with one of the farther O4″ atoms and is, therefore, bonded to six framework oxygens only (Fig. 6).

High-pressure behavior of triclinic scapolite

The *P*-induced evolution of the unit-cell parameters of triclinic scapolite is reported in Table S2 and Fig. 4. The bulk compression is mainly accommodated along the **b** and **c** crystallographic axes, whereas the **a** axis is apparently less affected by pressure. However, the compression along the [100] and [001] directions significantly increases in the higher pressure range (Fig. 4 and Table S2). As a consequence, a

change in the *V*–*P* pattern can be observed between 12.30 and 13.39 GPa, as confirmed by the change in the *P*-induced behaviors of the α and β crystallographic angles (Table S2). For this reason, no fit of the high-*P* behavior of the triclinic scapolite by an isothermal equation of state has been performed. The calculated average volume compressibility, $\overline{\beta_V} = -1/(\bar{V}) \cdot [(P_{max} - P_{min})/(V_{P_{max}} - V_{P_{min}})]$, is 0.0193 GPa^{-1}, in the *P*-range 10.08–12.30 GPa, and 0.0203 GPa^{-1}, in the range 13.39–17.79 GPa, respectively. A comparative analysis of the *P*-induced structure evolution of the triclinic scapolite, based on the structure refinements performed in the $I\bar{1}$ space group, is hindered by the high uncertainties of the refined parameters.

Discussion

Crystal chemistry and structure of the investigated scapolite

The results of the chemical analysis (Table 1) show that the investigated sample of scapolite has a composition intermediate between the end-members marialite and meionite, with a ratio (Na + K)/Si, which follows the compositional trend reported by Teerstra and Sheriff (1997). In addition, unit-cell parameters at ambient conditions also follow the trends reported by Sokolova and Hawthorne (2008) for the scapolite solid solution series. Unfortunately, no precise information on the origin of the investigated sample are available, but its chemical composition is quite close to those of sample "5" of Graziani and Lucchesi (1982) and sample "MAD" of Sheriff et al. (1998), both also from Madagascar. From the literature data (e.g., Teerstra and Sheriff 1997; Sheriff et al. 1998; Sokolova and Hawthorne 2008; Hawthorne and Sokolova 2008 and references therein), scapolites of intermediate composition are reported to crystallize in the primitive $P4_2/n$ tetragonal space group. However, the X-ray diffraction data collected on the single-crystal fragments of this study, using both conventional and synchrotron X-ray sources, do not show any evidence of violation of the *I*-centered reciprocal lattice (Fig. 3). From the structure refinement based on the intensity data collected with the crystal in air at the ESD-MI, the following average T–O bond distances can be calculated: 1.625(3) and 1.670(3) Å, for the T1 and T2 sites, respectively (Table 4). These values confirm that Al is preferentially ordered at the T2 site, but a minor fraction of this element also occupies the T1 site.

Transmission electron microscopy and electron diffraction data of primitive samples have shown the common occurrence of anti-phase domains of different size (e.g., Phakey and Ghose 1972; Oterdoom and Wenk 1983; Hassan and Buseck 1988; Seto et al. 2004). Oterdoom and Wenk (1983) suggest that, at an anti-phase boundary, a reversal of the ordering of the T2 and T3 sites, and of the related Si and Al distribution, occurs. Oterdoom and Wenk (1983) also suggest that anti-phase domains may form due to a transition from a disordered (i.e., *I*4/*m*) towards an ordered structure, or during the crystal growth. Seto et al. (2004) support the hypothesis that the anti-phase domains result from an *I*4/*m*-to-$P4_2/n$ phase transition induced by cooling, which implies that primitive scapolites of intermediate composition may crystallize in the *I*-centered space group at high temperature. The authors also suggest that a fast cooling may possibly lead to the persistence of a metastable *I*4/*m* scapolite at low temperatures, also at compositions where a primitive structure is expected. Hawthorne and Sokolova (2008) suggested that the size of the anti-phase domains would be a function of the cooling rate, where a faster cooling would lead to smaller domains, potentially undetectable by X-ray diffraction.

If the single-crystal fragments here investigated are the result of a significantly fast cooling, according to what suggested by Seto et al. (2004) and Hawthorne and Sokolova (2008), they would be characterized by very small anti-phase domains, with a reverse T2 and T3 ordering and a $P4_2/n$ structure. Due to the small size, these domains would not be detected by X-ray diffraction data, which will bear information of the average *I*4/*m* crystal structure. However, based on the collected data, we have no experimental basis to assert that the investigated sample is characterized by anti-phase domains with $P4_2/n$ structure, nor that, following the hypothesis of Seto et al. (2004), it is a metastable form of the *I*4/*m* structure preserved by a very fast cooling. For this reason, since a structure model based on the $P4_2/n$ space group would not be supported by the experimental X-ray diffraction data, the structure refinements of tetragonal scapolite have been performed in the *I*4/*m* space group. Nevertheless, the choice of the *I*4/*m* structure model does not induce any significant bias to the scopes of this study, i.e., (1) the determination of the isothermal elastic parameters of intermediate scapolite and (2) the description of the main mechanisms of structure deformation.

High-pressure behavior of intermediate scapolite

Hazen and Sharp (1988) first reported the isothermal elastic behavior of a meionitic scapolite (Me_{88}), with a bulk modulus of 90 GPa and an almost isotropic compressibility. The authors suggested that with an increasing Na content, the bulk compressibility would be significantly increased because of the higher compressibility of the Na–O bonds with respect to the Ca–O ones. Later, Comodi et al. (1990) reported the isothermal elastic behavior of two more sodic members, Me_{17} and Me_{68}, whose bulk moduli were refined to be 60 and 86 GPa, respectively, confirming the hypothesis of Hazen and Sharp (1988). In addition, if the bulk

compression of Me_{68} was found to be almost isotropic, like Me_{88}, in Me_{17} the structure along the **a** axis was clearly more compressible than along the **c** axis. The scapolite sample here investigated (Me_{47}) has a bulk modulus (70(2) GPa) that is intermediate between those of Me_{17} and Me_{68} (Fig. 4). In addition, the elastic anisotropy of our scapolite is also intermediate between Me_{17} and Me_{68}, further confirming that the Na content, which induces a channel expansion at ambient conditions (Papike and Stephenson 1966), favors the compression within the (001) plane and, therefore, the bulk compressibility of scapolite. Presently, our knowledge of the isothermal elastic parameters within the scapolite solid solution is limited to four members only and it is difficult to speculate on the deviation from the linear K_V vs % Me trend shown by either Me_{68} or Me_{88} (Fig. 4). Further investigations should be performed on the members of the scapolite solid solution series, with a special focus on samples close to the marialite and meionite end-members, in order to provide a robust description of the relationship between volume compressibility (β_V) and chemical composition.

The main deformation mechanism, which acts at the atomic scale, is the same already reported by Comodi et al. (1990) at high pressure, by Levien and Papike (1976) and Graziani and Lucchesi (1982) at high temperature and by Papike and Stephenson (1966) at varying chemical compositions, i.e., the rotation of the 4mRs around the shared O4 hinge, which induces the compression of the shorter diameter of the $8mR_{[001]}$ channels and, as a consequence, an increase in their ellipticity (Figs. 1, 5; Table 4). Coupled with the internal compression of the 4mR-II (Fig. 5; Table 4), this mechanism accommodates the bulk compression within the stability range of tetragonal scapolite. However, the saturating trend of these mechanisms is compensated, at $P > 4$ GPa, by the compression of the longest diameter of the $8mR_{[001]}$ channels (Figs. 1, 5; Table 4) and, partly, by the compression of the T2 tetrahedra. It is noteworthy to report that, at the same time, a saturation in the compressibility of the Ca–O2 and Ca–O4′ bonds is observed (Figs. 2, 5, Table S3). In addition to the increase in compressibility along the **c** crystallographic axis at $P > 2$ GPa, the observed deformation mechanisms suggest a destabilization of the tetragonal structure with increasing pressure, which leads to the phase transition to the triclinic polymorph. The structural cages hosting the anions were confirmed to act as relatively rigid units, as previously observed by Comodi et al. (1990), even if their compressibility increases with pressure, following the c vs. P behavior (see "High-pressure elastic behavior of tetragonal scapolite", "P-induced structure deformation of tetragonal scapolite").

Comodi et al. (1990) reported that the compressibility of the cation polyhedron increases with the Na content, being 68 GPa in Me_{68} and 46 GPa in Me_{17}, respectively. Due to the significant restrictions applied to the refinement of the CO_3 positions, we have calculated a fictive volume, defined as the cube of the average <Ca–Of> bond length, whose P-evolution (Table S3), at a first approximation, provides information on the compressibility of the cation polyhedron. A fit of the V–P data with a BM-EoS truncated to the second order, performed using the *EoS-Fit7_GUI* software (Angel et al. 2014; Gonzalez-Platas et al. 2016), leads to the following refined bulk modulus: $K_{V0} = 56(15)$ GPa, which is also intermediate between the values reported for Me_{17} and Me_{68}, respectively, by Comodi et al. (1990).

The $I4/m$-to-$I\bar{1}$ phase transition, due to the symmetry lowering, provides more degrees of freedom to the scapolite structure to accommodate compression, which is reflected by a slight increase in the bulk compressibility (Fig. 4). The bulk compression of the triclinic polymorph is mainly accommodated along the **b** and **c** crystallographic directions, which suggests a different behavior of the independent 8mRs. Unfortunately, the large uncertainties of the refined structural models do not allow an unambiguous comparative analysis of the structure deformation. The increase in compressibility at $P > 12.30$ GPa suggests an impending destabilization of the triclinic structure. Overall, the anomalous elastic behavior of the $I\bar{1}$ scapolite and the high pressure at which the phase transition occurs (at ambient temperature), apparently suggest that the triclinic polymorph is unlikely to occur in nature. In addition, based on the described deformation mechanisms acting at the atomic scale and on the elastic behavior of the tetragonal polymorph, a structural instability at $P > 2.0$–2.5 GPa (at ambient temperature) can be suggested. However, the absence of amorphization phenomena, at least up to 17.79 GPa, highlights the significant flexibility of the scapolite structure, which helps to understand why this mineral is so commonly found in rocks of different T and P origin, especially in the metamorphic realm.

Conclusions

Scapolites are volatile-bearing minerals widespread in metamorphic environments. Understanding the relative stability of scapolite in a mineral assemblage at varying pressures and temperatures may allow to reconstruct the formation conditions (e.g., Kullerud and Erambert 1999; Satish-Kumar et al. 2006; Hammerli et al. 2017). Modeling the stability of a mineral assemblage requires the knowledge of several thermodynamic parameters of the involved mineral phases, including the volume thermal expansivity, α_V, and compressibility, β_V (e.g., Almeida and Jenkins 2017). With regard to scapolites, this requires an experimental determination of these parameters across the solid solution series. In this work, we report the bulk volume compressibility (at ambient T) of a Me_{47} scapolite, which was found to be intermediate between the values reported in the literature for the Me_{17} and Me_{68} members (Comodi et al. 1990). Adopting the bulk modulus

refined from the II-BM EoS, for an ease of comparison with the literature data, a linear fit through the bulk moduli of Me_{17}, Me_{47}, Me_{68} and Me_{88} is possible. Taking into account all the limitations due to a linear fit based on four experimental points only, a rough extrapolation of the bulk moduli of the scapolite members in the range $Me_{17–88}$ is provided by the following equation: K_{V0} (GPa) = 53(2) + 0.45(4) × (% Me) [or β_V (GPa^{-1}) = 0.0179(6) − 0.00008(1) × (% Me)], where 17 ≤ % Me ≤ 88. Further mapping of the isothermal elastic behavior across the intermediate members of the scapolite solid solution is needed for better constraining the bulk modulus (and its pressure derivatives) as a function of the chemical composition, as provided, e.g., by Angel (2004) for plagioclase feldspars. Further investigations are also required for the compositions close to the marialite and meionite end-members, in order to observe possible deviations from the linear trend (cfr. Fig. 4). The experimental findings of this study also show an increase in the axial compressibility along the **c** axis at $P > 2.5$ GPa, which is followed by a re-arrangement in the structure deformation mechanisms at $P > 4$ GPa. Based on these data, a pressure limit (at room T) for the structural stability of scapolite may be inferred. However, robust extrapolations of the experimental structural data would be possible if further investigations on the behavior of scapolite solid solution members at high-(P, T) conditions will be provided and a comparative analysis would be possible.

From a broader point of view, the extrapolation of the elastic parameters as a function of the chemical composition may be applied to other solid solution series of minerals. In fact, the reported results further confirm that the substitution of Na by Ca in solid solutions of (open-)framework silicates is responsible for a decrease in the bulk compressibility at ambient conditions. This relationship has been experimentally observed across the plagioclase series by Angel (2004), but can also be observed in the group of fibrous zeolites (Gatta 2005), where Ca-rich scolecite (K_{V0} = 54.6(6) GPa) is stiffer than Na-rich natrolite (K_{V0} = 43(2) GPa), and in the group of sodalite, where the bulk modulus increases from the Na-rich (52(8) GPa; Hazen and Sharp 1988) to the Ca-rich end-members (69(6) GPa; Hargis et al. 2014).

Acknowledgements Two anonymous reviewers and the editor, Prof. Milan Rieder, are gratefully thanked for the valuable and fruitful comments and suggestions. Fernando Cámara and Andrea Risplendente (University of Milano) are thanked for the chemical analysis and Renato Pagano is gratefully thanked for providing the scapolite sample from his mineralogical collection. We acknowledge the European Synchrotron Radiation Facility for provision of synchrotron radiation facilities.

References

Almeida KMF, Jenkins DM (2017) Stability field of the Cl-rich scapolite marialite. Am Mineral 102:2484–2493

Angel RJ (2000) Equations of state. In: Hazen RM, Downs RT (eds) High-temperature and high-pressure crystal chemistry. Rev Mineral Geochem, vol 41. Mineralogical Society of America, Chantilly, pp 35–60

Angel RJ (2004) Equations of state of plagioclase feldspars. Contrib Mineral Petrol 146:506–512

Angel RJ, Bujak M, Zhao J, Gatta GD, Jacobsen SJ (2007) Effective hydrostatic limits of pressure media for high-pressure crystallographic studies. J Appl Crystallogr 40:26–32

Angel RJ, Alvaro M, Gonzalez-Platas J (2014) EosFit7c and a Fortran module (library) for equation of state calculations. Z Kristallogr 229:405–419

Arranz E, Lago M, Bastida J, Galé C (2002) Hydrothermal scapolite related to the contact metamorphism of the Maladeta plutonic complex, Pyrenees: chemistry and genetic mechanisms. Schweiz Miner Petrog 82:101–119

Baker J (1994) Thermal expansion of scapolite. Am Mineral 79:878–884

Baker J, Newton RC (1995) Experimentally determined activity-composition relations for Ca-rich scapolite in the system $CaAl_2Si_2O_8$–$NaAlSi_3O_8$–$CaCO_3$ at 7 kbar. Am Mineral 80:744–751

Bernal N, Gleeson SA, Smith MP, Barnes JD, Pan Y (2017) Evidence of multiple halogen sources in scapolites from iron oxide-copper-gold (IOCG) deposits and regional Na-Cl metasomatic alteration, Norrbotten County, Sweden. Chem Geol 451:90–103

Birch F (1947) Finite elastic strain of cubic crystals. Phys Rev 71:809–824

Chamberlain CP, Docka JA, Post JE, Burnham CW (1985) Scapolite; alkali atom configurations, antiphase domains and compositional variations. Am Mineral 70:134–140

Chervin JC, Canny B, Mancinelli M (2001) Ruby-spheres as pressure gauge for optically transparent high pressure cells. High Press Res 21:302–314

Comboni D, Gatta GD, Lotti P, Merlini M, Liermann H-P (2017) On the P-induced behavior of the zeolite phillipsite: an in situ single-crystal synchrotron X-ray diffraction study. Phys Chem Miner 44:1–20

Comodi P, Mellini M, Zanazzi PF (1990) Scapolites: variation of structure with pressure and possible role in the storage of fluids. Eur J Mineral 2:195–202

Duffy TS, Wang Y (1998) Pressure–volume–temperature equations of state. In: Hemley RJ (ed) Ultrahigh-pressure mineralogy. Rev Mineral Geochem, vol 37. Mineralogical Society of America, Chantilly, pp 425–458

Ellis DE (1978) Stability and phase equilibria of chloride and carbonate bearing scapolites at 750 °C and 4000 bar. Geochim Cosmochim Acta 42:1271–1281

Evans BW, Shaw DM, Haughton DR (1969) Scapolite stoichiometry. Contrib Mineral Petrol 24:293–305

Filiberto J, Treiman AH, Giesting PA, Goodrich C, Gross J (2014) High-temperature chlorine-rich fluid in the martian crust: a precursor to habitability. Earth Planet Sci Lett 401:110–115

Frietsch R, Tuisku P, Martinsson O, Perdahl J-A (1997) Early proterozoic Cu(-Au) and Fe ore deposits associated with regional Na-Cl metasomatism in northern Fennoscandia. Ore Geol Rev 12:1–34

Gatta GD (2005) A comparative study of fibrous zeolites under pressure. Eur J Mineral 17:411–421

Gatta GD, Lee Y (2014) Zeolites at high pressure: a review. Mineral Mag 78:267–291

Gatta GD, Lotti P (2016) Cancrinite-group minerals: crystal-chemical description and properties under non-ambient conditions—a review. Am Mineral 101:253–265

Gatta GD, Lotti P, Tabacchi G (2018) The effect of pressure on open framework silicates: elastic behaviour and crystal–fluid interactions. Phys Chem Miner 45:115–138

Gonzalez-Platas J, Alvaro M, Nestola F, Angel RJ (2016) EosFit7-GUI: a new graphical user interface for equation of state calculations, analyses and teaching. J Appl Crystallogr 49:1377–1382

Graziani G, Lucchesi S (1982) The thermal behavior of scapolite. Am Mineral 67:1229–1241

Hammerli J, Kemp AIS, Barrett N, Wing BA, Roberts M, Arculus RJ, Boivin P, Nude PM, Rankenburg K (2017) Sulfur isotope signatures in the lower crust: a SIMS study on S-rich scapolites on granulites. Chem Geol 454:54–66

Hargis CW, Moon J, Lothenbach B, Winnefeld F, Wenk H-R, Monteiro PJM (2014) Calcium sulfoaluminate sodalite ($Ca_4Al_6O_{12}SO_4$) crystal structure evaluation and bulk modulus determination. J Am Cer Soc 97:892–898

Hassan I, Buseck PR (1988) HRTEM characterization of scapolite solid solutions. Am Mineral 73:119–134

Hawthorne FC, Sokolova E (2008) The crystal chemistry of the scapolite-group minerals. II. The origin of the $I4/m \leftrightarrow P4_2/n$ phase transition and the nonlinear variations in chemical composition. Can Mineral 46:1555–1575

Hazen RM, Sharp ZD (1988) Compressibility of sodalite and scapolite. Am Mineral 73:1120–1122

Katongo C, Koller F, Ntaflos T, Koeberl C, Tembo F (2011) Occurrence and origin of scapolite in the neoproterozoic Lufilia-Zambezi Belt, Zambia: evidence/role of brine-rich fluid infiltration during regional metamorphism. In: Ray J, Sen G, Ghosh B (eds) Topics in igneous petrology. Springer, Dordrecht, pp 449–473

Kullerud K, Erambert M (1999) Cl-scapolite, Cl-amphibole, and plagioclase equilibria in ductile shear zones at Nusfjord, Lofoten, Norway: Implications for fluid compositional evolution during fluid-mineral interactions in the deep crust. Geochim Cosmochim Acta 63:3829–3844

Levien L, Papike JJ (1976) Scapolite crystal chemistry: aluminum–silicon distributions, carbonate group disorder, and thermal expansion. Am Mineral 61:864–877

Lin SB, Burley BJ (1973a) Crystal structure of a sodium and chlorine-rich scapolite. Acta Crystallogr B 29:1272–1278

Lin SB, Burley BJ (1973b) On the weak reflections violating body-centered symmetry in scapolites. Tschermaks Mineral Petrogr Mitt 20:28–44

Lin SB, Burley BJ (1975) The crystal structure of an intermediate scapolite – wernerite. Acta Crystallogr B 31:1806–1814

Lotti P, Gatta GD, Merlini M, Liermann H-P (2015a) High-pressure behavior of synthetic mordenite-Na: an in situ single-crystal synchrotron X-ray diffraction study. Z Kristallogr 230:201–211

Lotti P, Arletti R, Gatta GD, Quartieri S, Vezzalini G, Merlini M, Dmitriev V, Hanfland M (2015b) Compressibility and crystal–fluid interactions in all-silica ferrierite at high pressure. Micropor Mesopor Mater 218:42–54

Lotti P, Gatta GD, Comboni D, Merlini M, Pastero L, Hanfland M (2016) $AlPO_4$-5 zeolite at high pressure: crystal-fluid interaction and elastic behavior. Micropor Mesopor Mater 228:158–167

Mao HK, Xu J, Bell PM (1986) Calibration of the ruby gauge to 800 kbar under quasihydrostatic conditions. J Geophys Res 91:4673–4676

Mazhari SA, Amini S, Ghalamghash J, Bea F (2011) Metasomatic stages and scapolitization effects on chemical composition of Pasveh Pluton, NW Iran. J Earth Sci 22:619–631

Merlini M, Hanfland M (2013) Single-crystal diffraction at megabar conditions by synchrotron radiation. High Press Res 33:511–522

Miletich R, Allan DR, Kuhs WF (2000) High-pressure single-crystal techniques. In Hazen RM, Downs RT (eds) High-temperature and high-pressure crystal chemistry. Rev Mineral Geochem, vol 41. Mineralogical Society of America, Chantilly, pp 445–520

Momma K, Izumi F (2011) Vesta 3 for three-dimensional visualization of crystal, volumetric and morphology data. J Appl Crystallogr 44:1272–1276

Orville PM (1975) Stability of scapolite in the system Ab–An–NaCl–$CaCO_3$ at 4 kb and 750 °C. Geochim Cosmochim Acta 39:1091–1105

Oterdoom WH, Wenk H-R (1983) Ordering and composition of scapolite: field observations and structural interpretations. Contrib Mineral Petr 83:330–341

Papike JJ, Stephenson NC (1966) The crystal structure of mizzonite, a calcium- and carbonate-rich scapolite. Am Mineral 51:1014–1027

Pauling L (1930) The structure of some sodium and calcium aluminosilicates. Proc Natl Acad Sci 16:453–459

Petříček V, Dušak M, Palatinus L (2014) Crystallographic computing system JANA2006: general features. Z Kristallogr 229:345–352

Phakey PP, Ghose S (1972) Scapolite: observation of anti-phase domain structure. Nat Phys 238:78–80

Porter JK, Austrheim H (2017) Sulphide formation from granulite facies S-rich scapolite breakdown. Terra Nova 29:29–35

Rigaku Oxford Diffraction (2018) CrysAlisPro Software system, version 1.171.38.46. Rigaku Corporation, Oxford

Satish-Kumar M, Hermann J, Tsunogae T, Osanai Y (2006) Carbonation of Cl-rich scapolite boudins in Skallen, East Antarctica: evidence for changing fluid condition in the continental crust. J Metamorph Geol 24:241–261

Schiebold E, Seumel G (1932) Űber die Kristallstruktur von Skapolith. Z Kristallogr 81:110–134

Seto Y, Shimobayashi N, Miyake A, Kitamura M (2004) Composition and $I4/m$-$P4_2/n$ phase transition in scapolite solid solutions. Am Mineral 89:257–265

Shaw JM (1960) The geochemistry of scapolite. J Petrol 1:218–260

Sheriff BL, Sokolova EV, Kabalov YK, Teerstra DK, Kunath-Fandrei G, Goetz S, Jäger C (1998) Intermediate scapolite: ^{29}Si MAS and ^{27}Al SATRAS NMR spectroscopy and Rietveld structure-refinement. Can Mineral 36:1267–1283

Sheriff BL, Sokolova EV, Kabalov YK, Jenkins DM, Kunath-Fandrei G, Goetz S, Jäger C, Schneider J (2000) Meionite: Rietveld structure refinement, ^{29}Si MAS and ^{27}Al SATRAS NMR spectroscopy and comments on the marialite–meionite series. Can Mineral 38:1201–1214

Smith GC, Holness MB, Bunbury JM (2008) Interstitial magmatic scapolite in glass-bearing crystalline nodules from the Kula Volcanic Province, Western Turkey. Mineral Mag 72:1243–1259

Sokolova EV, Hawthorne FC (2008) The crystal chemistry of the scapolite-group minerals. I. Crystal structure and long-range order. Can Mineral 46:1527–1554

Sokolova EV, Kabalov YK, Sheriff BL, Teerstra DK, Jenkins DM, Kunath-Fandrei G, Goetz S, Jäger C (1996) Marialite: Rietveld structure refinement and ^{29}Si MAS and ^{27}Al satellite transition NMR spectroscopy. Can Mineral 34:1039–1050

Teerstra DK, Sheriff BL (1996) Scapolite cell-parameters trends along the solid-solution series. Am Mineral 81:169–180

Teerstra DK, Sheriff BL (1997) Substitutional mechanisms, compositional trends and the end-member formulae of scapolite. Chem Geol 136:233–260

Teerstra DK, Schindler M, Sheriff BL, Hawthorne FC (1999) Silvialite, a new sulfate-dominant member of the scapolite group with an Al-Si composition near the $I4/m$-$P4_2/n$ phase transition. Mineral Mag 63:321–329

Zolotarev AA (1993) Gem scapolite from the Eastern Pamirs and some general constitutional features of scapolite. Zapiski Vserossiiskogo Mineralogicheskogo Obshchestva 122:90–102 (In Russian).

Zolotarev AA (1996) Once more about the schemes and rows of isomorphism within the scapolite group. Zapiski Vserossiiskogo Mineralogicheskogo Obshchestva 125:69–73 **(In Russian)**